



Experimental study of liquid metal embrittlement for the aluminum 7075–mercury couple

Scott G. Keller, Ali P. Gordon*

Department of Mechanical, Materials & Aerospace Engineering, University of Central Florida, Orlando, FL, United States

ARTICLE INFO

Article history:

Received 14 May 2011

Received in revised form 10 January 2012

Accepted 1 February 2012

Keywords:

Fracture

Stress-intensity

Embrittlement

Incubation

Corrosion

ABSTRACT

Embrittlement of ductile structural members, whether under the presence of static or cyclic loading, can occur when surrounded by a corrosive environment. Several examples of catastrophic failures due to a form of environmentally assisted cracking (EAC) are available, with the failures of Liberty Ship hulls most commonly referred. Liquid metal embrittlement (LME) is a subset of EAC that results in the embrittlement of structural materials when intimately contacted by specific liquid metals. Several theories exist with the goal of identifying the key microstructural failure mechanism; however, most cannot account for all solid–liquid couples and do not incorporate a form of load dependency. Static and dynamic mechanical testing of notched and cracked specimens, respectively, was implemented to identify the dominant microstructural failure mechanisms and incorporate a load dependency on the life expectation of components. Results reveal crack initiation life behavior that is dependent on the time and load that the structural component remains subjected to LME conditions.

© 2012 Elsevier Ltd. All rights reserved.

1. Introduction

Environmental attack has led to the premature failure of structural components in a variety of industries, including maritime, aerospace and petrochemical processing [1–4]. Environmentally assisted cracking (EAC) describes a broad spectrum of cracking and embrittlement phenomena, including stress corrosion cracking (SCC), corrosion fatigue (CF), hydrogen embrittlement (HE) and liquid metal embrittlement (LME). Notable failures have occurred in which cracking of materials was aided by the environment, such as the Liberty Ships and Aloha Airlines Flight 243 failures [5]. Embrittlement via SCC and enriched salt environments has driven research in fracture mechanics and subsequently been applied to various other EAC phenomena [6]. Particular interest is in solid–liquid couples in which liquid materials degrade the ability of the solid material to resist fracture [7].

Liquid metal embrittlement is the inhibition of a solid metal to flow plastically when in intimate contact with a liquid metal. If proper wetting of the solid occurs, liquid metal reduces the fracture energy and fracture processes are more dependent on crack initiation; however, crack tip velocities have been investigated by various researchers, including Rhines et al. [8] Robertson [9], and Glickman [10]. Rhines and co-workers [8] use a simplistic pipe-flow model, suggesting the crack tip velocity is similar to that of the velocity of a fluid flowing through a pipe, i.e.,

$$v = \frac{\Delta p a^2}{8 \eta l}, \quad (1)$$

* Corresponding author.

E-mail addresses: scott.keller@ucf.edu (S.G. Keller), apg@ucf.edu (A.P. Gordon).

Nomenclature

a	pipe radius
B	thickness of fracture specimen
C_j	concentration of thermal kinks
C_0	equilibrium concentration of liquid
$C_{\infty L}$	equilibrium solubility
d	atomic diameter
D	diffusion coefficient
E	elastic modulus
f_m	moment correction factor
$f(a/w)$	geometric function
G	configurational force
h	crack width
H	diffusion length
k	boltzmann constant
K	strength coefficient
K_{Ic}	plane strain fracture toughness
K_t	stress concentration factor
l	length of pipe
n	hardening exponent
P_Q	peak load in calculating plane strain fracture toughness
S	nominal/remote stress
S_{gb}	grain boundary spreading effect
S_p	span distance
T	temperature
v	velocity
w	width of fracture specimen
β	constant
γ	surface energy
ΔP	difference in pressure
ε	notch tip strain
η	viscosity
θ	contact angle
σ_t	notch tip stress
ω, Ω	atomic volume

where Δp is the pressure difference, a is the radius of the pipe, η is the viscosity of the liquid metal and l is the length of the pipe. Robertson [9] describes the maximum crack tip velocity by a numerical constant, solid metal properties and the interaction of the two metals, i.e.,

$$v_{\max} = \frac{1}{2k} \frac{\Omega^2 E C_0 D}{d T}, \quad (2)$$

where k is the Boltzmann Constant, Ω is the atomic volume of the solid, E is the elastic modulus, d is the atomic diameter of the lattice atoms, C_0 is the equilibrium concentration of the liquid, D is the diffusion coefficient of the solute in the liquid and T is the temperature. The grain boundary crack velocity, as described by Glickman [10], is dependent on the equilibrium concentration of thermal kinks at the solid–liquid interface, C_j , the diffusion coefficient of the solid in the liquid, D_L , the equilibrium solubility of the solid in the liquid (given by the phase diagram), $C_{\infty L}$, the atomic volume, ω , configurational force, G , grain boundary spreading effect, S_{gb} , the crack width, h , and the characteristic diffusion length in the liquid phase, H , i.e.,

$$v = \left(\frac{C_j D_L C_{\infty L}}{kT} \right) \left[\frac{\omega(G + S_{gb})}{hH} \right]. \quad (3)$$

Each velocity model is dependent on various assumptions and mechanisms, developed fully in the body of each work. Experimental evidence is provided and correlates well with other independent works, where crack tip velocities were observed on the order of centimeters per second [11,12].

Not only do the crack tip velocity models differ with their assumptions, the underlying microstructural failure mechanism is still not fully understood. Various mechanistic models exist in effort to describe the crack tip driving force. Four particular models are briefly discussed here: the Decohesion model [13,14], Adsorption Induced Dislocation Emission (AIDE) model [15], Dissolution Condensation Mechanism (DCM) model [9,16], and the Grain Boundary Diffusion (GBD) model [17].

Of the most widely accepted models is the Decohesion model that was proposed by both Stoloff and Johnston [13] and Westwood and Kamdar [14]. Additionally, these two sets of researchers built upon the previous work of Nichols and Rostoker [18]. In dealing with the surface energy of the solid–liquid couple, the embrittling liquid would ultimately lower the cohesive strength of the solid metal, allowing for failure at a stress lower than the ultimate strength of the material, Fig. 1A. The theory does not account for any ductility, as the failure mode is considered to be a purely brittle fracture. Evidence of any ductility observed, either qualitatively or quantitatively, on the fracture surface would strongly oppose this theory.

The AIDE model, originally proposed by Lynch [15], allows for some plasticity ahead of the crack tip. Working along the lines of the Decohesion model, Lynch viewed fractured specimens under SEM and drew the conclusion that there was some plastic flow ahead of the crack tip, albeit reduced when compared to fractures in air, Fig. 1B. Through adsorption of the liquid metal, nucleation and egression of dislocations at the surface is facilitated, microvoids in the solid would be generated and coalesce to propagate the crack. The liquid environment would thus enable plastic flow through shearing of the atomic bonds, opposing the notion of the Decohesion model that no plastic flow was exhibited. Lack of ductile dimples on fractured surfaces would fail to provide substantial evidence of this theory.

The Dissolution Condensation Mechanism (DCM) model, an updated form of the Stress Assisted Dissolution model proposed by Robertson and Glickman, independently in the late 1960s, works in conjunction with Grain Boundary Wetting (GBW). Cracks can propagate under the application of an applied stress, albeit very small, through the mass diffusion of solid metal away from the crack tip, through either bulk-, grain boundary- or surface solid state diffusion, Fig. 1C. Fracture mechanics methods provide a means for an experimental platform in analyzing crack tip kinetics and the extension of an LME crack. Uncertainty in the mechanism arises when solubility in the liquid is nearly zero, as results for couples with little solubility in the liquid phase have been observed to have fast crack tip extension.

The Grain Boundary Diffusion (GBD) model provides evidence for the diffusion of liquid metals along the grain boundaries of solid metals. Through a reduction in strength of along the grain boundaries, components would fail intergranularly, i.e. decohesion of grain boundaries. Transgranular and cleavage-like fractures provide support that this model does not accurately describe all solid–liquid couples [19].

A variety of experimental routines have been implemented to study the effect of LME, in addition to the works mentioned previously [20–24]. These tests include standard tensile, delayed fracture, slow strain rate and fracture mechanics experiments. A majority of the works reported vital information on the crack tip behavior, most notably the crack tip velocity when exposed to the embrittling substance. Additionally, efforts have been made at understanding the time to rupture of components when subjected to a static stresses and stress intensities [25,26]. Results indicate that a general trend is apparent in the life, in that incubation periods precede subcritical crack growth periods and are followed by unstable crack growth/rupture, as generalized in Fig. 2 [27].

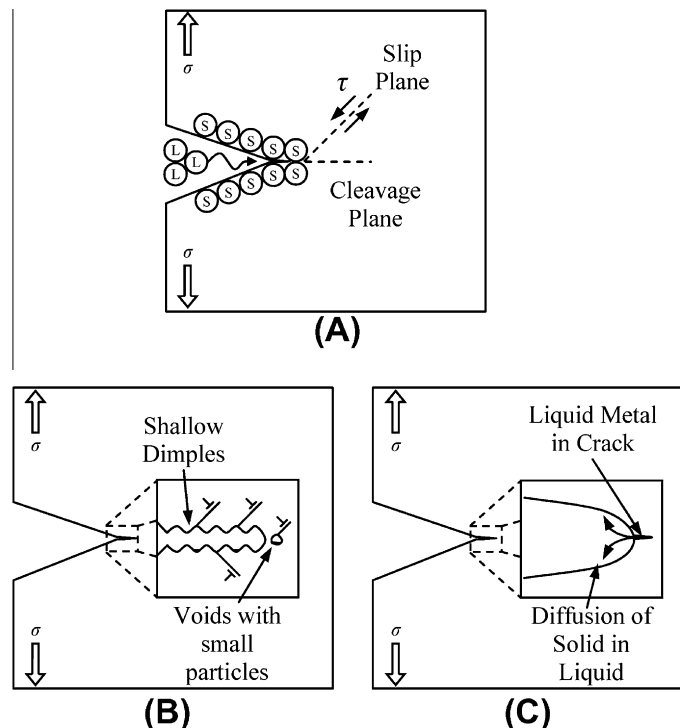


Fig. 1. Existing failure mechanisms regarding LME: Decohesion model (A), AIDE model (B) and the DCM model (C).

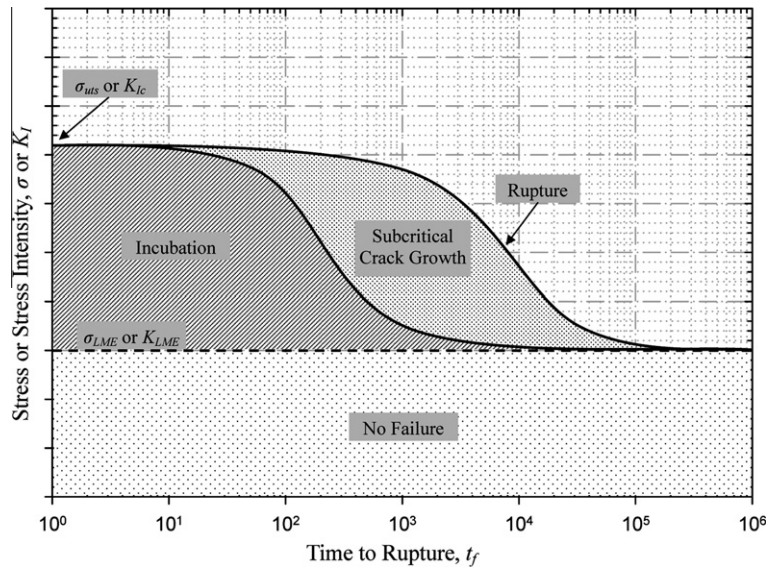


Fig. 2. Typical time to rupture plot of specimens subjected to static stresses and stress intensities.

While understanding the failure mechanism is of utmost importance in the design of equipment to be operated in the presence of embrittling materials, it is equally important to have the ability estimate the life of the component. Knowledge of the solid–liquid material couple should be well known, as well as the ultimate tensile stress, σ_{uts} , and the critical stress intensity, K_{Ic} , of the solid when in intimate contact with the liquid. As such, lives of notched and cracked specimens in a particular solid–liquid couple, representative of components found in design, are explored within the scope of this study.

The focus of the remainder of this study will focus on the development of experimental methods and the observed results. Along with these quantitative results from experiments, qualitative results from microscopy and related material analysis will be presented.

2. Experimental routines

Experimental routines aimed at determining the susceptibility of structural materials to LME are highly subjective to the solid–liquid couple used, as well as the test method employed. By controlling the materials and employing a variety of test routines, both initiation and propagation processes are able to be observed.

For this study, an aluminum alloy, Al 7075-T651, known for its high strength and susceptibility to EAC was chosen as the solid metal. Selected mechanical properties and chemical composition are provided, Tables 1 and 2, respectively. The liquid embrittler chosen was liquid mercury, as the solubility parameter difference between the two metals is high, resulting in less of an interaction between the solid and liquid metals [28]. By limiting the amount of interaction between the solid–liquid couple, emphasis can be placed on the stress-related interactions instead of the material interactions, such as diffusion of liquid into the solid.

Sessile drop experiments assist in characterizing the interaction between a solid–liquid couple, as information about the surface energies is readily attainable. Through contact angle measurements of a sessile drop on a solid surface, as shown in Fig. 3, Young's equation, i.e.,

$$\gamma_{SV} = \gamma_{SL} + \gamma_{LV} \cos \theta, \quad (4)$$

and the Equation of State, i.e.,

Table 1
Mechanical properties of Al 7075-T651 in air [39,40].

	S–L	T–L	L–T
Yield strength, σ_y (MPa (ksi))	430 (62.5)	489 (70.9)	498 (72.3)
Ultimate strength, σ_{uts} (MPa (ksi))	462 (67.1)	540 (78.3)	563 (81.7)
Rupture strain, ϵ_f (%)	1.32	4.8	6.27
Fracture toughness, K_{Ic} (MPa \sqrt{m} (ksi \sqrt{in}))	17.6 (16.0)	24.2 (22.0)	28.6 (26.0)
Elastic modulus, E (GPa (Msi))	–	–	71 (10.3)
Poisson's ratio, ν	–	–	0.33

Table 2

Chemical composition of Al 7075-T651, wt.%.

Al	87.1–91.4	Mg	2.1–2.9	Zn	5.1–6.1
Cr	0.18–0.28	Mn	Max 0.3	Ti	Max 0.2
Cu	1.2–2	Si	Max 0.4	Fe	Max 0.5

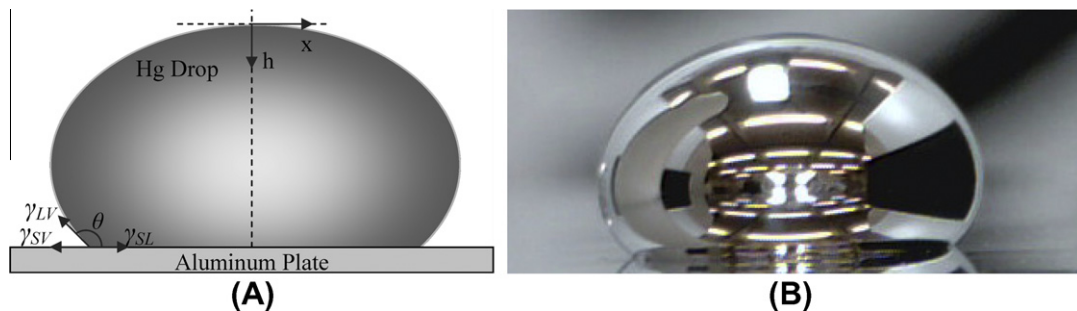


Fig. 3. Sessile drop technique that utilizes the contact angle to calculate the surface energies (A) and an example of a liquid Hg drop on an Al 7075-T651 plate specimen (B).

$$\gamma_{SL} = \gamma_{LV} + \gamma_{SV} - 2\sqrt{\gamma_{LV}\gamma_{SV}}e^{-\beta(\gamma_{LV}-\gamma_{SV})^2}, \quad (5)$$

can be simultaneously solved to provide the surface energy of the solid when in contact with the liquid. In these equations, γ is surface energy and the subscripts relate to the surface tension between the solid–vapor, γ_{SV} , solid–liquid, γ_{SL} , and the liquid–vapor, γ_{LV} . θ is the contact angle the drop makes on the surface and β is a constant [29]. Utilizing drop experiments, the contact angle at the solid–liquid interface can be measured and related back to the surface energy [26]. Coupling these observations with the strain-energy release, rupture of the solid when exposed to the liquid can be approximated.

Time to rupture curves can be generated for a variety of controlling quantities, with the focus on two for this particular study; stress and stress intensity. The first controlling quantity, stress, can be obtained either by smooth or notched tensile specimens, while the latter is achieved by using fracture mechanics specimens with a mechanically generated crack. By observing the time a smooth or notched specimen, without the presence of a crack, resists rupture, a critical stress for the particular solid–liquid couple can be associated with crack initiation processes. Through fracture mechanics specimens, either compact tension ($C(T)$) or four-point bending $C(B)$, and blunt notch tensile specimens, the propagation of an existing crack can be monitored and used to determine the amount of subcritical crack growth. Upon rupture, the two sets of time-dependent rupture data can indicate remaining life for the corresponding solid–liquid couple.

Experiments were carried out on two uniaxial test frames; a MTS Insight electromechanical frame utilizing customized TestWorks4 routines and a MTS servohydraulic frame with the Teststar IIs controller. Combined, the two frames are capable of statically and dynamically loading specimens, either via displacement-, strain- or load-rate, and maintaining desired stress/strain levels. Stress-based experiments were primarily conducted on the electromechanical frame, whereas experiments based on stress intensity were conducted on the servohydraulic frame.

Specimens were machined out of Al 7075-T651 plate in the S – L orientation, Fig. 4. Two specimens were primarily used in this investigation, namely a notched tensile specimen and a $C(T)$ fracture specimen, Fig. 5. The notched tensile specimen incorporates a stress concentration of 1.87 at the notch tip, as calculated by common formulae [30]. Normalizing the stress facilitated at the notch root of each specimen, without the presence of a crack, the influence of the stress concentration on each specimen is provided as a function of the distance from the geometric discontinuity, as shown in Fig. 6. In un-cracked specimens, a $C(T)$ specimen that is subjected to a bending moment, denoted as $C(B)$, has the most steep stress gradient and the notched tensile specimen has the least. The inclusion of $C(B)$ specimens is relevant in this study and will be developed in more detail shortly.

The notches in tensile specimens were generated through standard machining practices while the starter notches for $C(T)$ and $C(B)$ specimens were generated via EDM machining. An additional polishing process was taken for notched tensile specimens, such that notch roots were polished with cotton twine immersed in a 0.5 μm alumina solution while rotating in a lathe to reduce the number of micronic stress risers. As notch roots were already smooth as machined, this process of polishing allowed for minimal removal of material, while having the ability to remove the oxide layer, which is expected to be only several atomic radii thick [31].

The presence, or lack thereof, of an oxide layer will influence the results obtained in experiments; as such, the amount of time between polishing and testing will be discussed further in Section 4. Each specimen was machined in the S – L orientation so that the crack would propagate in the direction of rolling (e.g. L), through the center of the plate and have a uniform microstructure ahead of the desired crack path. Furthermore, data regarding this orientation is not as widely available as it is for other orientations, i.e. T – L or L – T .

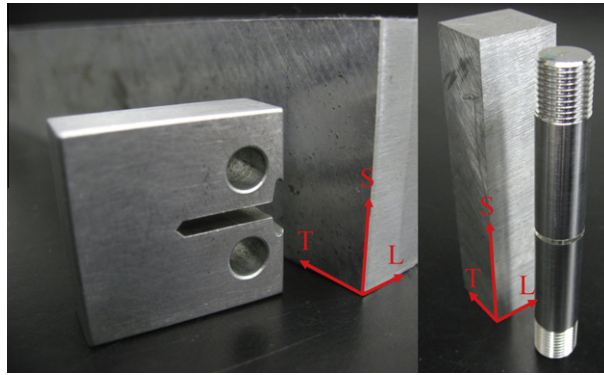


Fig. 4. S–L-oriented compact tension (left) and S-oriented notched tensile (right) specimens used in the experimental portion of this study.

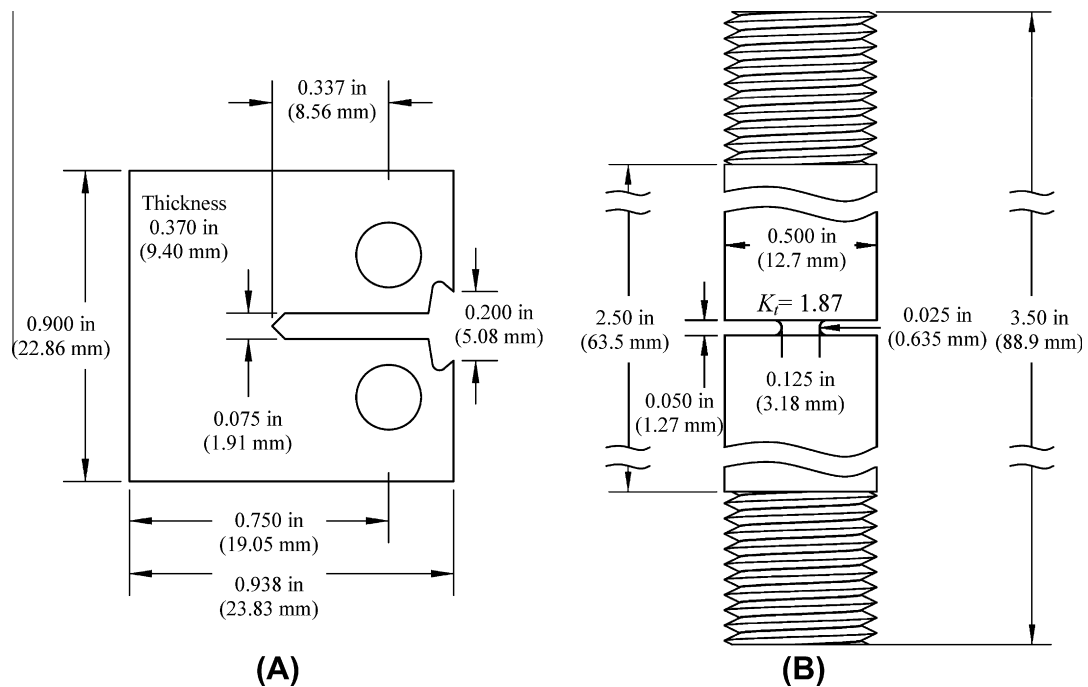


Fig. 5. Dimensions of the C(T) and notched tensile specimens used in the current study.

Stress-based time to rupture experiments, loaded via load control, involved forming a disposable environmental chamber around the notch, capable of subjecting the highly stressed region to liquid mercury, Fig. 7. An extensometer (MTS Model #634.11E-25) was used to directly measure the remote elongation and strain. In the event of plasticity at the notch tip, local stress is approximated by solving Neuber's rule and the Ramberg–Osgood relationship simultaneously through an iterative process. Neuber's rule makes use of the nominal stress and strain concentration factor, i.e.,

$$\sigma_t \varepsilon_t = \frac{(K_t S)^2}{E}, \quad (6)$$

where σ_t is the local notch tip stress, ε_t is the local notch tip strain, K_t is the stress concentration factor, S is the remote or nominal stress and E is the elastic modulus [32]. During plastic deformation, the stress–strain nonlinearity is approximated through the Ramberg–Osgood equation, e.g.,

$$\varepsilon = \frac{\sigma}{E} + \left(\frac{\sigma}{K}\right)^{\frac{1}{n}}, \quad (7)$$

where K is the strength coefficient and n is the strain hardening exponent, both of which are material constants [33]. Utilizing a Newton–Raphson iteration technique, Eqs. (6) and (7) can be solved simultaneously to approximate the notch tip engi-

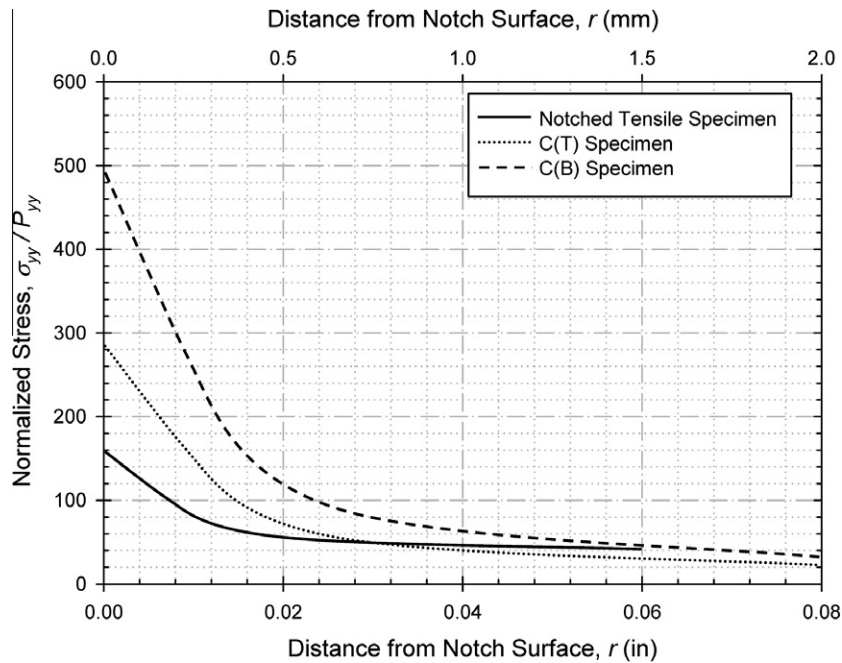


Fig. 6. Influence of the stress concentration as a function of the distance from the geometric discontinuity for the three specimens used in this study.

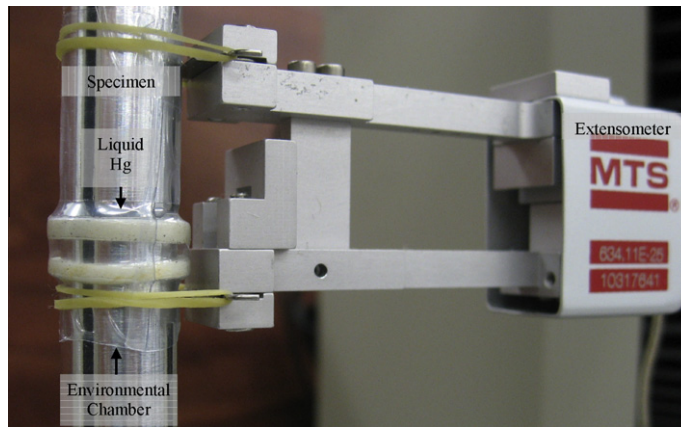


Fig. 7. Experimental setup for notched tensile specimens, with disposable environmental chamber, liquid Hg in the notch and extensometer.

neering stress and strain. Approximation of local strains was provided by extensometry at the remote section, as it was assumed that any extension would be a result of deflection in the reduced section due to difference in stresses experienced at the nominal and gross cross-sections.

Stress-based load control experiments involved stepped-load routines that utilized five load steps, with an incubation time at each step. Upon reaching the final load, the routine would maintain the final load until rupture or run-out, which was 10^6 s (or 11.57 days). It was expected that routines with higher load steps would result in shorter rupture times. Stepped-load histories provide the advantage of being able to observe the effect plasticity has in rupture processes in a single test and the influence plasticity has on LME.

Stress intensity-based experiments required the development of a new method of applying load and liquid embrittler to the specimen. Pursuant to plane-strain fracture toughness testing, particularly ASTM E399, test configurations can be implemented, including tensile or three-point bending apparatus can be used [34]. Initial testing was conducted under typical tensile loading, in which $C(T)$ specimens were completely submerged in liquid Hg, as detailed in [35]. Subsequent tests were conducted using a modified four-point with the objective of enabling the use of standard $C(T)$ fracture specimens and in doing so, rendering them as $C(B)$ specimens, Fig. 8. Most notably, this design allows for the incorporation of a clip gage (MTS Model #632.02E-20) capable of directly measuring crack tip opening displacement (CTOD). Stress intensities for

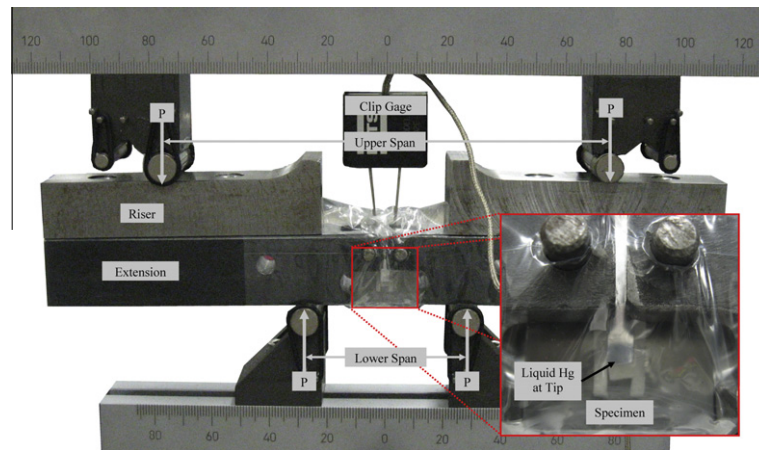


Fig. 8. Experimental setup for $C(B)$ specimens in the modified four-point bending apparatus, with liquid Hg at the starter notch and clip gage for CTOD measurements.

$C(T)$ and $C(B)$ specimens were calculated based on the plane-strain fracture toughness equation after a mechanically developed crack of length a was generated, e.g.,

$$K_I = \frac{P_Q}{B\sqrt{W}} \cdot f\left(\frac{a}{W}\right), \quad (8A)$$

$$K_I = \frac{P_Q S_p f_m}{B\sqrt{W}} \cdot f\left(\frac{a}{W}\right), \quad (8B)$$

where P is the load, S_p is the span distance, f_m is a moment correction factor, B is the thickness, W is the width and $f(a/W)$ is a geometric function based on the fracture specimen and ratio of crack length to width. The moment correction factor, f_m , is used to account for the difference between applied moments in three- and four-point bending, which equated to 0.65 for current experiments.

Both the stress- and stress intensity-based time to rupture curves were conducted via load control conditions. Fracture mechanics specimens were pre-cracked in the liquid environment followed immediately by the incubation period, without removal from liquid Hg in between. Upon reaching a predetermined load, or approximate stress intensity, the frame would then maintain load and allow the specimen to incubate until complete rupture or run-out, whichever was achieved first. Estimations of the stress intensity due to the crack are used; however, after rupture, actual values were calculated based on post-mortem analyses.

Post-mortem analyses were conducted on samples from each type of test. Along with macroscopic images, scanning electron microscopy (SEM) images were taken on select fracture specimens fractured in air and liquid Hg environments. Additionally, energy dispersive X-ray (EDX) was used on specimens fractured in liquid Hg to ensure liquid embrittler was present at various locations on the fracture surface. Together, post-mortem analyses assisted in understanding the failure mode of aluminum subjected to LME conditions.

3. Experimental results

Sessile drop experiments revealed consistent contact angles between the polished aluminum plates and liquid Hg. Drops of varying mass were placed on the surface, all of which resulted in a contact angle of approximately 128° . The corresponding surface energy for the solid–liquid couple, γ_{SL} , using Eqs. (4) and (5), is 210 mJ/m^2 . In calculating the effective surface energy, as in [26], the solid–liquid surface energy is insignificant in comparison to the plastic deformation work.

Similar to $S-N$ curves used in fatigue life analyses, typical time to rupture plots employ a static load until rupture of the specimen is noted. In this study, a constant stress intensity was maintained on compact fracture specimens while a constant notch tip stress was maintained on notched tensile specimen until failure, Figs. 9 and 10, respectively.

Constant stress intensity to failure time provided a mixture of results, with rupture occurring at various times during the loading regime, as shown in Fig. 9. Here, specimen prefixes denote the test method used, where SL -identifies conventional $C(T)$ specimens and CTB -identifies specimens that utilized the four-point method. Some specimens were observed to fracture upon mechanical precracking (not included in results), initial load application, after an incubation period or did not rupture and were considered to be a “run-out.” Additionally, some specimens were observed to rupture at locations other than the fatigue starter notch, whether a fatigue pre-crack was present or not, which were not included in the results [35]. Such results were the motive behind the modified four-point bend assembly, as well as further rounding the fillet at the knife edge valley, as shown in Fig. 5.

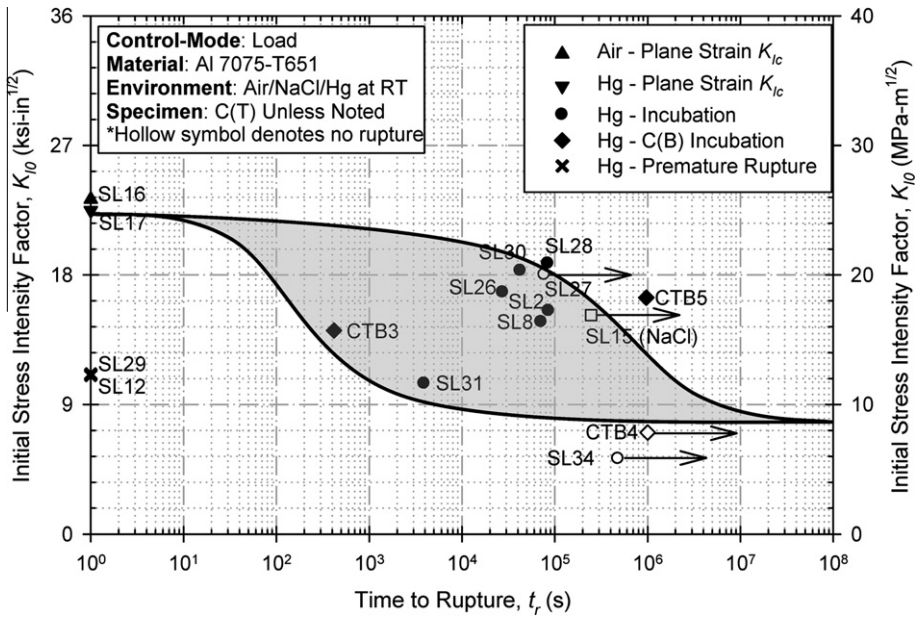


Fig. 9. Incubation life for static stress intensity experiments on Al 7075-T651 in Hg.

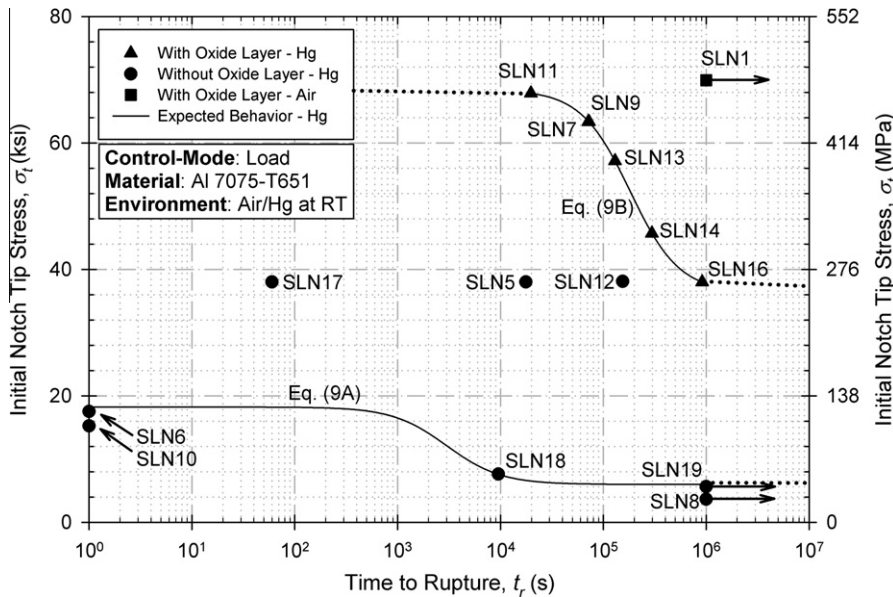


Fig. 10. Incubation life for static notch stress experiments on Al 7075-T651 in Hg.

Constant notch tip stress to failure plots provided similar results, with some specimens rupturing upon the initial load and others sustaining load for a period of time, as shown in Fig. 10. Specimens that were polished and immediately tested revealed a large amount of scatter in the time to rupture plot. With a severely diminished, or nonexistent, oxide layer, LME conditions are more readily achieved, i.e., intimate wetting of the aluminum surface by the mercury. Rupture of specimens appeared random, with no discernable trend. Some specimens ruptured during the initial load ramp, while others lasted almost the entirety of the allotted test time, similar to results for SIF-based incubation.

4. Discussion

Resistance to rupture of fracture specimens, whether in air or in liquid Hg, yielded similar results, as K_{Ic} was measured as 23.51 ksi $\sqrt{\text{in}}$ (25.84 MPa $\sqrt{\text{m}}$) and 22.74 ksi $\sqrt{\text{in}}$ (24.99 MPa $\sqrt{\text{m}}$), for air and Hg environments, respectively. Plane strain

fracture toughness values were obtained were from $C(T)$ specimens with starter notch formed by EDM and from relatively thin sheets of aluminum (1.0 in. or 2.54 cm). The sessile drop data provided evidence that the effective surface energy is insignificantly affected by the addition of mercury to the surface. The dominating factor is the plastic work done during mechanical loading. As such, an insignificant drop in the fracture toughness, as observed, is expected. Additionally, it is known that the elastic response of the material is not affected in the embrittling environment [36]. The plane strain fracture toughness is captured under the premise of nominally elastic response at the crack tip and it is therefore reasonable to believe that a significant drop in the plane strain fracture toughness is not expected.

Furthermore, environmentally assisted cracking is a highly time-dependent process, which requires a period of time for interaction between solid and liquid metals. During the plane strain fracture tests, results are obtained instantaneously, not permitting a sufficient amount of interaction time between the two metals. In order to determine the effect on the plane strain fracture toughness, presoaking specimens for a period of time prior to conducting a test could reveal a more dramatic drop in the plane strain fracture toughness value. Critical pre-exposure times can be obtained through such a routine. This experimental procedure will be investigated in a future study.

In SIF-based incubation experiments (Fig. 9), a few specimens failed prior to expected incubation times, as noted by an “X” on the K_{I0} -axis at $t_0 = 1$ s. These specimens lasted the entirety of the pre-cracking routine only to rupture upon ramping to the static load. Displacements and loads remained nearly constant up until complete fracture of the specimen occurred. Complete rupture was observed to occur in less than 0.1 s, as such, crack growth data was not able to be extrapolated, as the sampling frequency was 10 Hz. The crack was able to extend through the width of the specimen before a subsequent data point was captured, but expected to be consistent with previous research [23,24]. As such, the crack tip velocity models presented, Eqs. (1)–(3), were unable to be directly validated in this particular study.

Analyzing the incubation data points, it was observed that experiments conducted under similar conditions ruptured at various times which provided an assortment of results. Some specimens, e.g. S-L-26, S-L-8, were able to maintain an initial SIF and rupture as expected, while other specimens either fractured upon load application, as mentioned previously, or were halted, e.g. S-L-27. It is proposed that the reason the experiments contain as much variation as observed is directly related to the severity of macro-cracks at the starter notch. Depending on the surface roughness or a small flaw in the material, several cracks can initiate. If these cracks are sufficiently close to one another, the complex state of stress at each tip can overlap one another, creating a more severe state of stress; however, if the cracks are far enough apart, this will not happen. Overlapping stress fields will result in crack propagation at lower SIFs, while a single crack will behave significantly different.

Notched tensile specimens were observed to display a similar trend as $C(T)$ specimens, in that some specimens ruptured during initial load while others lasted the entirety of the allotted test time. Incubation times are provided, with the designation between identical specimens with or without a developed oxide layer, as shown in Fig. 10. Specimens that were allowed to rest in lab air upon polishing and prior to testing were observed to have a higher incubation life by an order of magnitude and greater. Upon differentiation between specimens that were polished and tested immediately as opposed to specimens that sat prior to testing, a trend among the specimens was apparent.

Macroscopic analysis supported data provided by extensometry for both types of specimens in regards to plastic deformation. When compared to specimens fractured in air, fracture mechanics specimens ruptured in Hg appeared to have a more brittle fracture and tended to exhibit cleavage-like fracture, as shown in Fig. 11A and B. A majority of $C(T)$ specimens exhibited fracture surfaces that were mostly smooth and appeared relatively flat; however, some specimens exhibited large delaminations throughout the region in contact with the liquid embrittler. These steps are attributed to intergranular delamination, as observed for the Al 7075-T651-Hg couple in 1989 [37]. Tensile specimens subjected to liquid Hg displayed similar differences to specimens ruptured in air, as shown in Fig. 11C and D.

Cracks were observed to occur at various locations along the starter notch height and the machined notch in fracture mechanics and notched tensile specimens, respectively. Provided the specimen orientation, more than 7000 grain boundaries were available in the S direction along the starter notch, using average grain thicknesses of $7\ \mu\text{m}$ ($275\ \mu\text{in}$), as provided by Zhao and Jiang [38]. Similarly, more than 1800 grain boundaries were available in the S direction in the notched tensile specimens. No specific trends were observed in specimens that had crack initiation in locations other than the expected location of crack initiation/propagation. With this high concentration of grain boundaries along the notches, it provides evidence that LME could potentially be grain boundary-dependent and this orientation provides for multiple locations that provide favorable crack initiation conditions.

Due to the notched tensile test specimen geometry, traditional stress–strain curves cannot be directly produced, only notch root stress and strain can be approximated. Therefore, plasticity in specimens fractured in air was observed via load–displacement curves, as well as visually observing the reduction area. When fractured in liquid Hg, the elastic response was similar; however, the reduction area was less, signifying less ductility.

Specimens that fractured during the initial load ramp, SLN6 and SLN10, had no discernible differentiating features between fracture surfaces. Both samples displayed burn markings (notably darker, soot-like appearance as shown in Fig. 11B and D), as well as relatively flat fracture surfaces. Previous investigation of rupture times were observed to be near instantaneous, with some scatter among points, suggesting that a similar trend would be observed if more experiments were performed within similar time frames [36]. Future experiments will emphasize testing within this short time span in effort to provide accurate life approximations for a variety of loads and environments.

A key identifying feature of specimens fractured in liquid Hg was the appearance of burn marks. Fracture specimens were observed to have dark, “burnt” patches on the fracture surface, as well as extensive cracking along the profile of the spec-

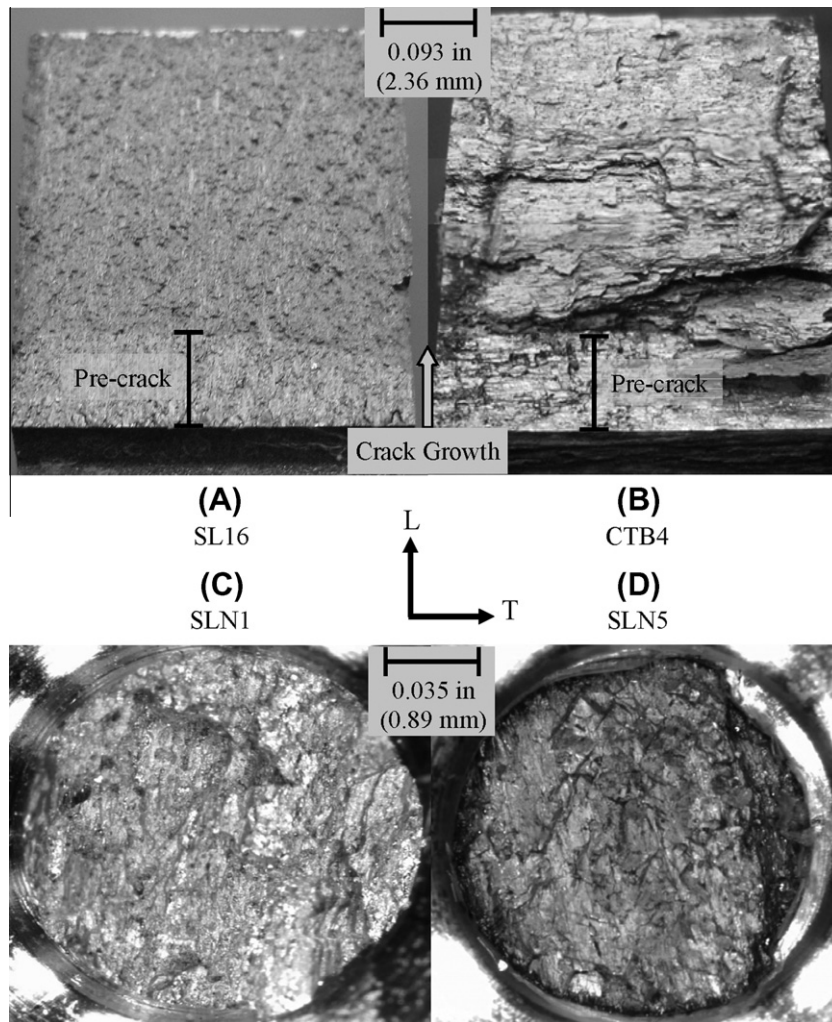


Fig. 11. Comparison of fracture surfaces for $C(T)$ specimens and notched tensile specimens fractured in air (A and C) and liquid Hg (B and D).

imen, which were not observed on specimens ruptured in air, Fig. 12A and B. As mentioned previously, large amount of delamination of grains is observed, notably Fig. 12B. Notched tensile specimens ruptured in air lacked the burn markings on the fracture surface, as well as burnt areas on the stress-free surface away from the notch, Fig. 12C and D. The appearance of these dark regions will be discussed further.

Scanning electron microscopy was utilized on selected fracture specimens. Specimens ruptured in lab air environments displayed intergranular fracture, with the presence of dimples in several regions whereas specimens ruptured in liquid Hg revealed mostly brittle features, most notably cleavage-like fracture, as shown in Fig. 13. In small regions, dimples were observed on the cleavage-like surfaces. The presence of dimples on specimens ruptured in mercury is significant in that it provides support for the AIDE mechanism and detracts from the Decohesion mechanism. To ensure that these regions were exposed to the embrittler, energy dispersive X-ray spectroscopy (EDX) aimed at these areas revealed trace amounts of mercury.

In the current study, subcritical crack growth was not observed in $C(T)$, $C(B)$ or K_r specimens. Upon imposing a sustained load, elongation as measured by the clip gage or extensometer was observed to remain constant. Fracture specimens that remained at load failed to show any increase in the crack tip opening displacement. For notched tensile routines, elongations were only noted during load advancement from one step to the next during a single incubation experiment. As most of the expected notch tip stresses were within the elastic region of the material, the elongation was noted as linear between each load step.

The influence of the oxide layer significantly affected the life of the notched specimen when subjected to an embrittling environment. Regardless of the failure mechanism, the oxide layer blocks the intimate wetting that is necessary for LME conditions to occur, as noted by the delayed rupture of specimens with an oxide layer present prior to testing. It is proposed that the life of the oxide barrier is then the critical element in life estimation and upon rupture of this layer, intimate wetting of

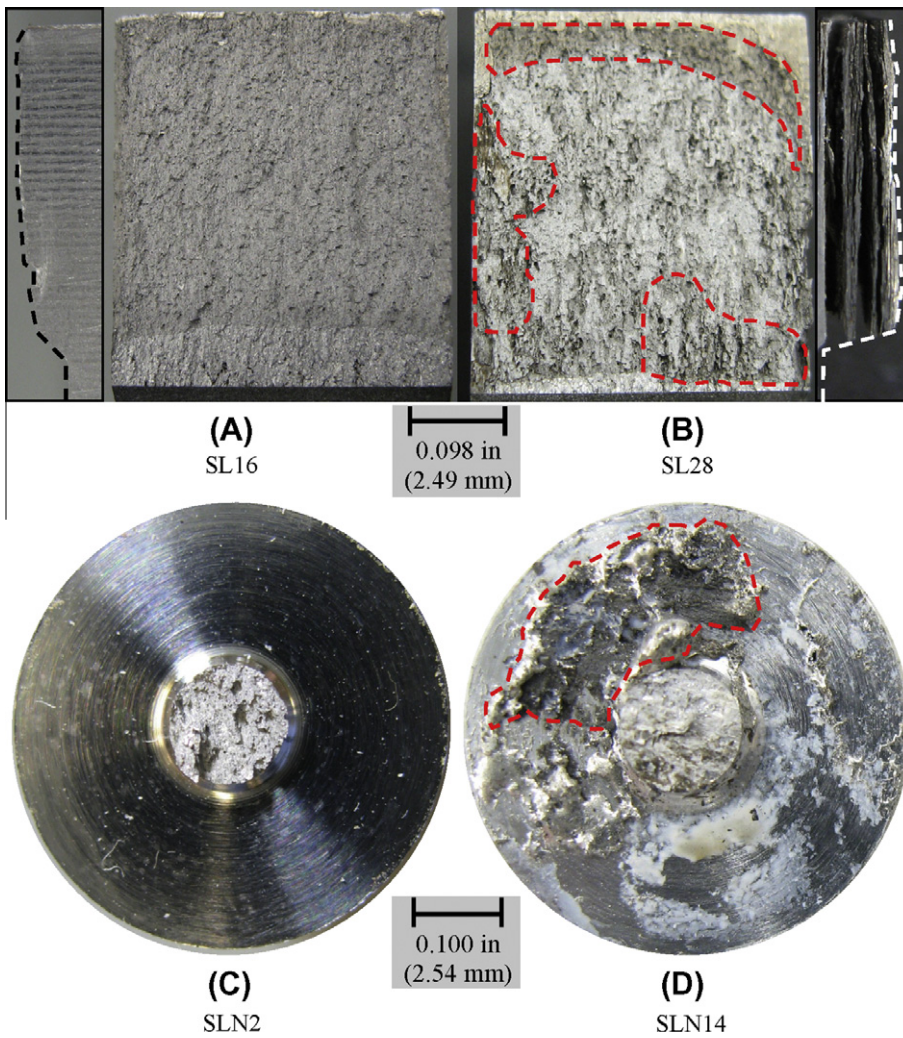


Fig. 12. Crack profile and surface conditions for $C(T)$ and notched tensile specimens fractured in air (A and C) and liquid Hg (B and D), in which burnt regions are highlighted.

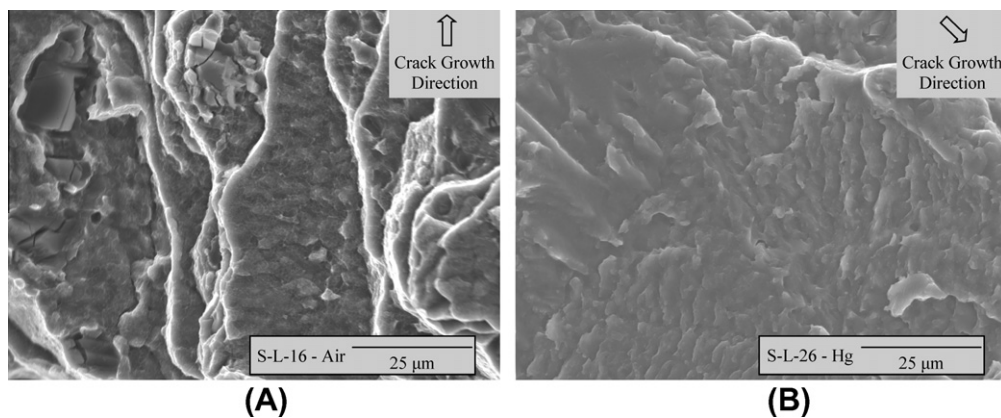


Fig. 13. SEM image of a $C(T)$ fracture surface in which mostly brittle-like cleavage fracture is apparent.

the solid metal occurs. In this scenario, with the applied notch tip stress well above the LME threshold for this particular solid–liquid couple, rupture is expected to occur simultaneously.

Life predictions can be for notched tensile specimens based upon the two distinct groups of data in Fig. 10, i.e., specimens with or without an oxide layer. Even with significant differences in rupture life, the trend for each subset is expected to be identical. The life of the component can be expected to be a product of the ultimate strength, σ_{uts} , LME threshold strength, σ_{LME} , notch tip stress, σ_t , rupture time, t_r and two additional parameters, m and q , i.e.,

$$\sigma_t = \sigma_{LME} + \frac{\sigma_{uts} - \sigma_{LME}}{1 + \left(\frac{t_r}{m}\right)^{-q}}, \quad (9A)$$

$$\sigma_{t,ox} = \sigma_{LMEox} + \frac{\sigma_{uts} - \sigma_{LMEox}}{1 + \left(\frac{t_r}{m_{ox}}\right)^{-q_{ox}}}. \quad (9B)$$

The two additional terms, m and q , are the fitting parameters that correspond to the median effective concentration of data and the slope of the curve at the location of m , respectively. Distinction between Eqs. (9A) and (9B) lies in the addition of “ox” to the subscripts, as this differentiates between specimens that have no oxide layer or a developed oxide layer, respectively. It should be noted that the analytical model is highly dependent on the solid–liquid couple used, as well as the surface conditions, and relies heavily on experimental data, as noted by the difference between values in Table 3.

Life predictions for fracture mechanics specimens are expected to follow the time to rupture curves, as shown in Fig. 2, and analytically represented similarly by Eq. (9). As such, two bounds have been superimposed over the rupture life data in Fig. 9. In place of the critical stress values, a critical stress intensity, K_{crit} , as well as a lower limit threshold stress intensity, K_{LME} , will be substituted. The constants are defined by the data, and as such, more data is necessary to provide meaningful constants.

Eq. (9) should not be considered an “all inclusive” life prediction model, as there are several factors that are distinct to the particular solid–liquid couple. The notion of a LME threshold, either σ_{LME} or K_{LME} , is not novel, nor is it trivial for every solid–liquid couple. To date, the only reliable method of establishing the LME threshold known to the authors is through mechanical experimentation. In notched tensile specimens with a developed oxide layer, it should be noted that the lower limit is not the LME threshold, as rupture was observed at far lower stress levels when no oxide layer was present, as shown in Fig. 10.

Results in Fig. 10 reveal that specimens with a developed oxide layer resist loads approximately 3.5 times greater than those of specimens without an oxide layer. If the oxide layer is absent, interaction between the mercury and aluminum is readily observed, as the oxide layer acts as the barrier to inhibit diffusion into the solid metal. This constitutes the necessary wetting conditions and thereby reducing the load carrying capability by activating the LME process. For specimens with the oxide barrier, over time, it is expected to break due to the mechanical loading, thus providing the necessary wetting conditions required for LME processes to activate. The breakdown of the oxide layer is time-dependent, as well, which leads to the longer rupture times for specimens with the protective oxide layer.

The possibility of a threshold stress based on the life of the oxide layer is presented, as noted in Eq. (9B) by $\sigma_{LME,ox}$. Upon reaching this level, the specimen is expected to rupture, as the necessary conditions for wetting are provided and true LME conditions exist. As no discernable specimen elongation was observed, as measured by the extensometer, it is proposed that a breakdown of the oxide layer and rupture of the specimen occur simultaneously, as notch stresses were already above the true LME stress threshold. A direct result of this process is the absence of subcritical crack growth.

The instantaneous rupture, as well as the small scale plasticity, helps to identify a failure mechanism for this particular solid–liquid metal couple. The Decohesion mechanism relies on a purely brittle fracture via reduced atomic bonds. The localized plasticity observed on surfaces fractured in mercury suggests that this mechanism may not be best suited for this couple. Conversely, it lends support for the AIDE mechanism [15], as it is similar to the Decohesion model [13,14]; however, allows for small plasticity ahead of the crack tip and advances through microvoid coalescence. Cleavage-like features on SEM images detract from the GBD mechanism, which suggests fracture via intergranular means.

The remaining mechanism under investigation, the Dissolution Condensation Mechanism [9,16], has unique evidence in this study. One of the main features of this particular mechanism is that the embrittling liquid acts as a transport vessel for solid metal atoms to move away from the crack tip to be re-deposited on stress-free surfaces. On several notched tensile specimens, burn markings previously noted on the rupture surface were observed to occur away from the notch root along the stress free portion of the machined slot, as shown in Fig. 12. These burn markings, highlighted in the dotted regions, provide evidence that the liquid metal potentially acts as a transport media for corroded solid material to vacate the advancing crack tip. Chemical analysis of the burned regions is necessary to confirm these findings without uncertainty.

Table 3
Constant used in Eq. (9).

	OX	Non-OX
σ_{LME} – lower limit	68.4	18.2
m – median concentration	181814.6	3001.3
q – slope at m	–1.8	–1.6

Overall, rupture of specimens was expected to occur instantly upon crack initiation or crack propagation. No discernible trend was observed when LME conditions prevailed. The inability to definitely label the trends lies in the scatter that is inherent to environmentally assisted cracking investigations. A multitude of factors can affect the life of components with active competition between the true failure mechanisms, which results in significant scatter among data for a variety of solid–liquid couples. It was noted, however, that when an oxide layer was present, the life of the oxide layer was the determining factor in life estimation. As for the mechanism, qualitative data tends to support a mixture of the AIDE and DCM failure mechanisms.

5. Conclusions

Liquid metal embrittlement has been observed in the Al 7075–T651–Hg solid–liquid metal couple. Through fracture mechanics and notched tensile specimens, the life of “service-like” components subjected to a static stress intensity or notch tip stress, respectively, has been assessed. Results show that rupture is imminent upon crack initiation or crack propagation, unless a barrier exists, such as an oxide barrier, that prevents intimate wetting required for LME conditions. Sessile drop experiments provided surface energy measurements and estimations of K_{ILME} were consistent with values obtained via fracture mechanics experiments. A life prediction model was developed based on experimental evidence that is capable of rupture prediction for notched tensile components subjected to a sustained static load. Metallurgical analysis was used to identify key features on fracture surfaces, used in indentifying the underlying failure mechanism. In regards to the failure mechanism, this particular couple shows evidence of a combination of the Adsorption Induced Dislocation Emission and the Dissolution Condensation Mechanism models. Continuing efforts will be made to differentiate between the mechanisms and to indentify the leading microstructural failure mechanism.

References

- [1] Lynch SP. Failures of structures and components by environmentally assisted cracking. *Engng Fail Anal* 1994;1(2):77–96.
- [2] Lynch SP. Failures of engineering components due to environmentally assisted cracking. *Pract Fail Anal* 2003;3(5):33–42.
- [3] Lynch SP. Failures of structures and components by metal-induced embrittlement. *J Fail Anal Prevent* 2008;8(3):259–74.
- [4] English JJ, Korbin G. Liquid mercury embrittlement of aluminum. *Mater Perform* 1989;28(2):62–3.
- [5] Johnson R. Aging aircraft and structural airworthiness. *SAE Trans* 1991;100(1):2731–48.
- [6] Sumpter JDG, Kent JS. Prediction of ship brittle fracture casualty rates by a probabilistic method. *Mar Struct* 2004;17(1):575–89.
- [7] Malu MK, Preece CM. The role of solute additions to aluminum on its embrittlement by mercury. *Mater Sci Engng* 1973;11(4):223–6.
- [8] Rhines FN, Alexander JA, Barclay WF. The mechanism of mercury stress-crack propagation in 70/30 brass and 2024-ST4 aluminum. *Trans ASM* 1962;55(1):22–44.
- [9] Robertson WM. Propagation of a crack filled with liquid metal. *Trans Met Soc AIME* 1966;236(10):1478–82.
- [10] Glickman EE. Fast penetration of Ga in Al: liquid metal embrittlement near the threshold of grain boundary wetting. *Int J Mater Res* 2005;96(10):1204–10.
- [11] Benson BA, Hoagland RG. Crack growth behavior of a high strength aluminum alloy during lime by gallium. *Scrip Metall* 1989;23(11):1943–8.
- [12] Kapp JA, Duquette D, Kamdar MH. Crack growth behavior of aluminum alloys tested in liquid mercury. *J Eng Mater Technol* 1986;108(1):37–43.
- [13] Stoloff NS, Johnston TL. Crack propagation in a liquid metal environment. *Acta Metall* 1963;11(4):251–6.
- [14] Westwood ARC, Kamdar MH. Concerning liquid metal embrittlement, particularly of zinc monocrystals by mercury. *Philos Mag* 1963;8:787–804.
- [15] Lynch SP. Effect of environment on fracture – mechanisms of liquid–metal embrittlement, stress-corrosion cracking and corrosion-fatigue. *Int Conf Fract* 1977;1:859–66.
- [16] Glickman EE, Goryunov YV. Mechanism of embrittlement by liquid metals and other manifestations of the rebinder effect in metal systems. *Sov Mater Sci* 1978;14(4):355–64.
- [17] Krishtal MA, Vyobyschik MA, Sudnik VA. Diffusion of impurity atoms along dislocations in aluminum. *Phys Met Metall* 1973;36(5):191–3.
- [18] Nichols H, Rostoker W. Mercury embrittlement of an Al–4 ½ pct Mg alloy. *Trans ASM* 1964;230(1):251–3.
- [19] Wanhill RJH. Cleavage of aluminum alloys in liquid mercury. *Corrosion* 1974;30(10):371–8.
- [20] Kane RD, Wu D, Wilhelm SM. Use of slow strain rate tests to evaluate the embrittlement of aluminum and stainless alloys in process environments containing mercury. *ASTM STP* 1993;1210:181–92.
- [21] Gordon P, An HH. The mechanisms of crack initiation and crack propagation in metal-induced embrittlement of metals. *Met Trans A* 1982;13A(3):457–72.
- [22] Krupowicz JJ. Slow strain rate fracture characteristics of steel and aluminum alloys tested in mercury environments. *J Eng Mater Technol* 1989;111(3):229–34.
- [23] Wheeler DA, Hoagland RG, Hirth JP. Effect of solid metal strength level on the liquid metal embrittlement of aluminum by mercury. *Scripta Metall* 1988;22(4):533–8.
- [24] Wheeler DA, Hoagland RG, Hirth JP. Evidence for crack tip oxidation effects during the liquid metal embrittlement of AA 7075 aluminum alloy by mercury. *Corrosion* 1989;45(3):207–12.
- [25] Gordon P. Metal-induced embrittlement of metals – an evaluation of embrittler transport. *Met Trans A* 1978;9A(2):267–73.
- [26] Chu WY, Liu XM, Lou JL, Qiao LJ. Mechanism of embrittlement of Al alloy by liquid metal (Ga). *Can Met Q* 1999;32(2):127–32.
- [27] Janssen M, Zuidema J, Wanhill R. *Fracture mechanics*. 2nd ed. New York: Spon Press; 2004.
- [28] Kamdar MH. Liquid–metal embrittlement. *Met Hdbk* 1987;11:171–84.
- [29] Tavanaa H, Neumann AW. Recent progress in the determination of solid surface tensions from contact angles. *Adv Colloid Interface Sci* 2007;132(1):1–32.
- [30] Pilkey WD. *Peterson’s stress concentration factors*. 2nd ed. New York: John Wiley & Sons; 1997.
- [31] Jeurgens LPH, Sloof WG, Tichelaar FD, Borsboom CG, Mittemeijer EJ. Determination of thickness and composition of aluminum-oxide overlayers on aluminum substrates. *Appl Surf Sci* 1999;144:11–5.
- [32] Knop M et al. On the Glinka and Neuber methods for calculating notch tip strains under cyclic load spectra. *Int J Fatigue* 2000;22(9):743–55.
- [33] Stephens RI, Fatemi A, Stephens RR, Fuchs HO. *Metal fatigue in engineering*. 2nd ed. New York: John Wiley & Sons; 2001.
- [34] ASTM Standard E399. Standard test method for linear-elastic plane-strain fracture toughness, K_{Ic} , of metallic materials. *ASTM Int* 1990; 1997.
- [35] Keller SG, Gordon AP. An experimental approach for delayed stress corrosion. In: *PVP2010 Proc* 2010.
- [36] Sadananda K, Vasudevan AK. Review of environmentally assisted cracking. *Met Trans A* 2011;42A(2):279–95.

- [37] Liu Y, Hoagland RG. Transient and intermittent crack growth during embrittlement of 7075-T651 aluminum by mercury. *Scripta Metall Mater* 1989;23(3):339–44.
- [38] Zhao T, Jiang Y. Fatigue of 7075-T651 aluminum alloy. *Int J Fatigue* 30(5):834–49.
- [39] Jiang Y. Stress corrosion of AISI 4340 steel and 7075-T651 aluminum alloy. In: *ONR wksp New York*; June, 2009.
- [40] ASM International. *Properties and selection: non-ferrous alloys and special-purpose materials*. 7th ed. vol. 2. Materials Park: ASM Intl; 2007.